Detailed Analysis of Two Particle Correlations in Central Pb-Au Collisions at 158 GeV per Nucleon

Vom Fachbereich Physik
der Technischen Universität Darmstadt

zur Erlangung des Grades
eines Doktors der Naturwissenschaften
(Dr. rer. nat.)

genehmigte Dissertation von
Dariusz Antończyk
aus Krakau

Darmstadt 2006
(D 17)

Referent: Prof. Dr. P. Braun-Munzinger
Koreferent: Prof. Dr. J. Wambach

Tag der Einreichung: 18.10.2006
Tag der Prüfung: 20.12.2006

Abstract

This thesis presents a two-particle correlation analysis of the fully calibrated high statistics CERES Pb+Au collision data at the top SPS energy, with the emphasis on the pion-proton correlations and the event-plane dependence of the correlation radii. CERES is a dilepton spectrometer at CERN SPS. After the upgrade, which improved the momentum resolution and extended the detector capabilities to hadrons, CERES collected 30 million Pb+Au events at 158 AGeV in the year 2000. A previous Hanbury-Brown-Twiss (HBT) analysis of pion pairs in a subset of these data, together with the results obtained at other beam energies, lead to a new freeze-out criterion [AAA+03]. In this work, the detailed transverse momentum and event-plane dependence of the pion correlation radii, as well as the pion-proton correlations, are discussed in the framework of the blast wave model of the expanding fireball.

Furthermore, development of an electron drift velocity gas monitor for the ALICE TPC sub-detector is presented. The new method of the gas composition monitoring is based on the simultaneous measurement of the electron drift velocity and the gas gain and is sensitive to even small variations of the gas mixture composition. Several modifications of the apparatus were performed resulting in the final drift velocity resolution of 0.3 permille.

Zusammenfassung

In der vorliegenden Arbeit untersuchen wir Zweiteilchenkorrelationen und die Abhängigkeit der Korrelationsradien von der Orientierung zur Reaktionsebene in Schwerionenstößen. Eine solche Analyse wird hier zum ersten Mal anhand der vollständig kalibrierten Daten des CERES Detektors zu Pb+Au Kollisionen bei maximaler Strahlenergie am CERN SPS durchgeführt. CERES, ursprünglich als Dileptonenspektrometer konzipiert, verfügt nach der Erweiterung um eine Zeitprojektionskammer über die Möglichkeit Hadronen zu rekonstruieren sowie über verbesserte Impulsauflösung. In der vorliegenden Arbeit untersuchen wir Datenzu 30 Millionen Pb+Au Kollisionen bei 158AGeV aus dem Jahr 2000. Die kombinierten Ergebnisse einer Hanbury-Brown-Twiss (HBT) Analyse von Pionpaaren aus einer früheren Analyse eines Teils der vorliegenden Daten und Ergebnisse von anderen Strahlenergien resultieren in einem neuen Kriterium für den thermischen freeze-out [AAA+03]. In dieser Arbeit diskutieren wir die Systematik der rekonstruierten Pionenkorrelationsradien in Abhängigkeit vom Transversalimpuls und der Orientierung relativ zur Stossebene sowie die Pion-Proton-Korrelationen im Rahmen eines "blast wave" Modells des expandierenden Feuerballs.

Ein weiterer Schwerpunkt dieser Arbeit besteht in der Weiterentwicklung einer Apparatur zur Überwachung der Driftgeschwindigkeit in Gasmischungen für die ALICE Zeitprojektionskammer. Zahlreiche Veränderungen zur Verbesserungen der Driftgeschwindigkeitsmessung

4

wurden vorgenommen um eine Auflösung von 0.3 Promille zu erreichen. Das neue Verfahren zur präzisen Kontrolle der Zusammensetzung der Mischung über die Driftgeschwindigkeit und den Gasverstärkungsfaktor erlaubt es, minimale Abweichungen der Mischungsverhältnisse vom Sollwert nachzuweisen.

Contents

List of Figures

List of Tables

xiii

Chapter 1

Introduction

Ultra-relativistic heavy ion collisions offer a unique possibility to examine the properties of the strongly interacting matter. The description of such interacting many-body system at high energy densities ϵ is given by the nonperturbative quantum chromodynamics (QCD). For the energy density of $\epsilon \approx 1$ GeV/fm^3 the calculations predict a phase transition from a state formed by hadrons to a new state of deconfined quarks and gluons [CP75, Pol78] called the Quark Gluon Plasma (QGP) [Shu78, McL86]. The transition is accompanied by the restoration of the chiral symmetry which is spontaneously broken in the QCD ground state. It is believed that free quarks and gluons existed as the QGP in the Early Universe up to few microseconds after the Big Bang [Oli91]. It has also been suggested that cold and highly compressed QGP may exist in the core of neutron stars [EKO91b, EKO91a]. Understanding of the evolution and properties of the new state of matter created during ultra-relativistic heavy ion collisions would provide a deeper insight into these aspects of cosmology.

Experiments at the Alternating Gradient Synchrotron (AGS), the Super Proton Synchrotron (SPS), and the Relativistic Heavy Ion Collider (RHIC) were and still are looking for signatures of the QGP formation [MAT89, MAT04, MAT06]. It is a challenging task taking into account the diameter of the reaction volume of several fermi and the very short life time of the QGP state, about 5-10 fm/c. Moreover, the signals coming from the QGP are combined with those emitted from the hot hadronic gas phase and thus a combination of various signatures may be needed to conclude whether the quark-gluon plasma was created or not.

The CERES spectrometer was set up at the CERN SPS facility in order to investigate heavy-ion collisions with the focus on the measurement of the low-mass e^+e^- pairs emitted in proton- and ion-induced collisions at ultra-relativistic energies. After upgrade with the Time Projection Chamber the experiment extended its capability to hadronic signatures of the hot and dense matter. This work focuses on the systematic study of the two-particle correlations created during collisions of Pb-Au nuclei at 158 GeV/c per nucleon. The two-particle correlation technique provides access to the information about the space-time geometry and the dynamics

of the collision region and allows to determine the relative emission times or positions of the different particle species.

1.1   Strongly Interacting Matter

The theory of the strong interaction, called quantum chromodynamics (QCD), describes the forces between the colored particles, quarks and gluons. Two remarkable properties of this theory are the *asymptotic freedom* and the *confinement*. The strength of the strong interaction is given by the QCD running coupling constant $\alpha_s\left(\mathsf{q}^2\right)$, which depends on the momentum transfer q

$$\alpha_s\left(\mathsf{q}^2\right) = \frac{4\pi}{\left(11 - \frac{2}{3}n_f\right)\ln\left(\frac{\mathsf{q}^2}{\Lambda_{QCD}^2}\right)}\,, \tag{1.1}$$

where n_f is the number of flavors with mass below $\sqrt{|\mathsf{q}^2|}$ and Λ_{QCD}^2 is the QCD scale parameter introduced in the renormalization process. In the limit of $\alpha_s\left(\mathsf{q}^2\right) \to 0$ the coupling strength between colored particles is vanishing resulting in free quarks and gluons. Expressing the $\alpha_s\left(\mathsf{q}^2\right)$ in terms of the coordinate space r, the coupling strength grows like r^2. Therefore, at large distances the binding between quarks grows giving rise to a strong attractive force confining quarks into hadrons. The quark model introduced by Gell-Mann and Zweig, based on the symmetries and quantum numbers, categorized hundreds of particles states known at that time [GM64]. They postulated that all hadrons are built from smaller constituents called quarks. All hadrons are divided into two groups, called mesons and baryons. Mesons are composed of a quark and anti-quark $(q\bar{q})$ while baryons consist of three quarks (qqq) or $(\bar{q}\bar{q}\bar{q})$. The quarks occur in six *flavors*: u, d, s, c, t, b, have spin $1/2$, and are ruled by the Fermi-Dirac statistics. Since some of the baryons consist of three identical quarks, an additional quantum number was introduced, called *color*, in order to preserve the Pauli principle. There are three different colors a quark can carry, say *red*, *green*, and *blue*. All observed hadrons are colorless (or white) and can be constructed either from *color-anti color* (mesons) or three different *colors* (baryons). Gluons, the *color-charged* field quanta of the strong interaction, can have eight different color states. Therefore, QCD is a gauge theory based on the SU(3) color symmetry group.

Based on the fundamental properties explained above, QCD predicts a transition from a state formed by hadrons to a plasma of deconfined quarks and gluons, at a sufficiently high energy density [CP75, Pol78]. The transition energy density is a few GeV/fm^3 compared with 0.15 GeV/fm^3 of nuclear matter in its ground state. Lattice QCD calculations predict that such transition should be accompanied by the chiral symmetry restoration which is spontaneously broken at low temperatures [LW74]. Below the critical temperature (T_c) quarks are confined in hadrons with dynamically generated masses of a few hundred MeV. The expectation value of the *quark condensate* $\left\langle\bar{\psi}\psi\right\rangle \approx -(235 \text{ MeV})^3$ describes the density of $q\bar{q}$ pairs in the QCD

vacuum and the fact that it is not vanishing is directly related to the chiral symmetry breaking [Kar02]. Lattice QCD calculations show that around the critical temperature the effective masses of quarks are no longer given by the dynamically generated masses but rather by their current masses. In the limit of zero current quark masses the quark condensate is vanishing and chiral symmetry is restored. The results of such calculation are shown in Fig. 1.1. Based on these calculations and on the simple physical intuition one can sketch the phase diagram of strongly interacting matter shown in Fig. 1.2. The hatched band in the temperature vs. baryon chemical potential plane (T, μ_b) there represents a boundary between a gas of hadronic resonances at low energy densities and a QGP phase at high energy densities [BMS02]. The phase transition between QGP and hadronic matter is thought to be of first order at non-vanishing μ_b. However, as $\mu_b \to 0$ quark masses become significant and a sharp phase transition transforms into a rapid but smooth cross-over. The hadrochemical freezeout points are determined from thermal model analysis [BMSWX96, BMHS99] of heavy ion collision data at SIS, AGS, and SPS energy [Sta99, BM00]. The arrow connection the chemical and the thermal freeze-out curves at the SPS corresponds to isentropic expansion.
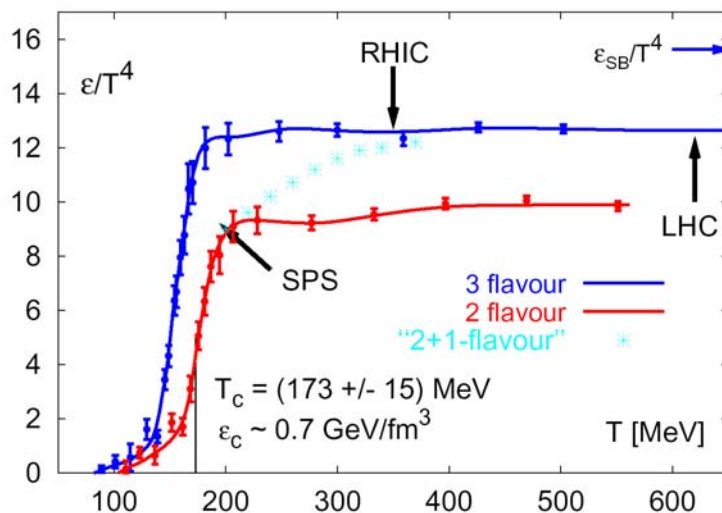
Figure 1.1: Energy density ϵ/T^4 as a function of T with $n_f = 2, 3$ light quarks as well as two light and one heavier (strange) quarks [KL03]. Arrows depict the energy densities reached in the initial stage of heavy ion collision at the SPS, RHIC, and also for the LHC based on the Bjorken formula (see Eq. 1.19). The arrow parallel to the temperature axis indicate the ideal gas limit.
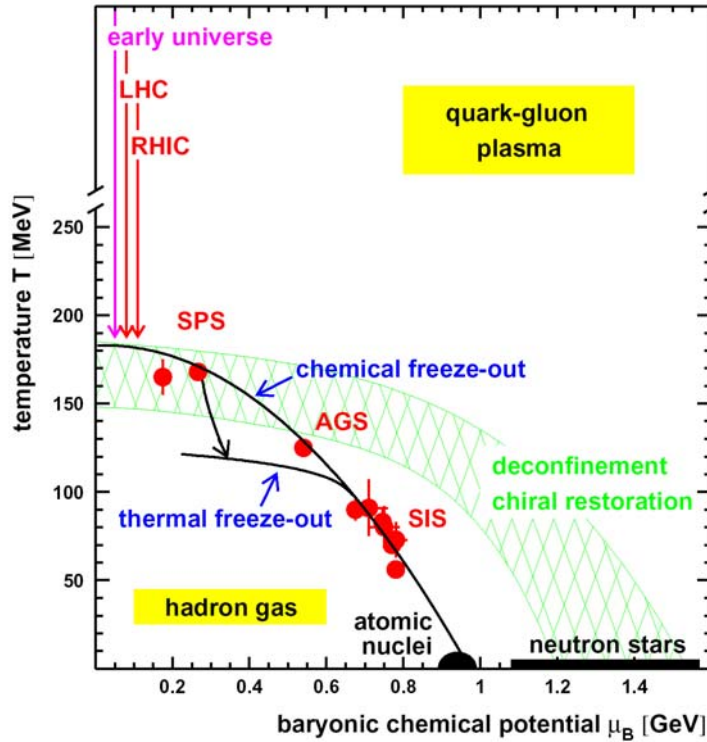
Figure 1.2: Phase diagram of hadronic matter [BM00].

1.2   Heavy Ion Collision Experiments

First heavy ion experiments were performed in the sixties in nuclear emulsions exposed to cosmic-ray nuclei in balloon flights. During that time, first ideas and methods were created to analyze such data which are used still nowadays. In the late sixties, acceleration of heavy ions began. The generation of proton synchrotrons at CERN, Brookhaven, and Protvino at that time reached few hundred MeV/c per nucleon. The accelerators operating nowadays can reach collision energies up to 40 TeV, for the heaviest colliding systems, with a high beam luminosity. That opens a great opportunity to study different colliding systems for various beam energies, and to explore the phase diagram of nuclear matter in hunt for the QGP.

The space-time evolution of an ultrarelativistic heavy ion collision is shown in Fig. 1.3. Due to the Lorentz contraction the colliding nuclei are highly compressed in the beam direction. At the first instants of the collision, called *pre-equilibrium*, the energy deposited in the collision volume is redistributed into other degrees of freedom. After the time $\tau \approx 1$ fm/c (*formation time*) the deposited energy may lead to the formation of the QGP. At this stage one can assume that the system is in thermal equilibrium, and thus the further evolution of the system can be described in terms of hydrodynamical models. The pressure inside the hot and dense medium
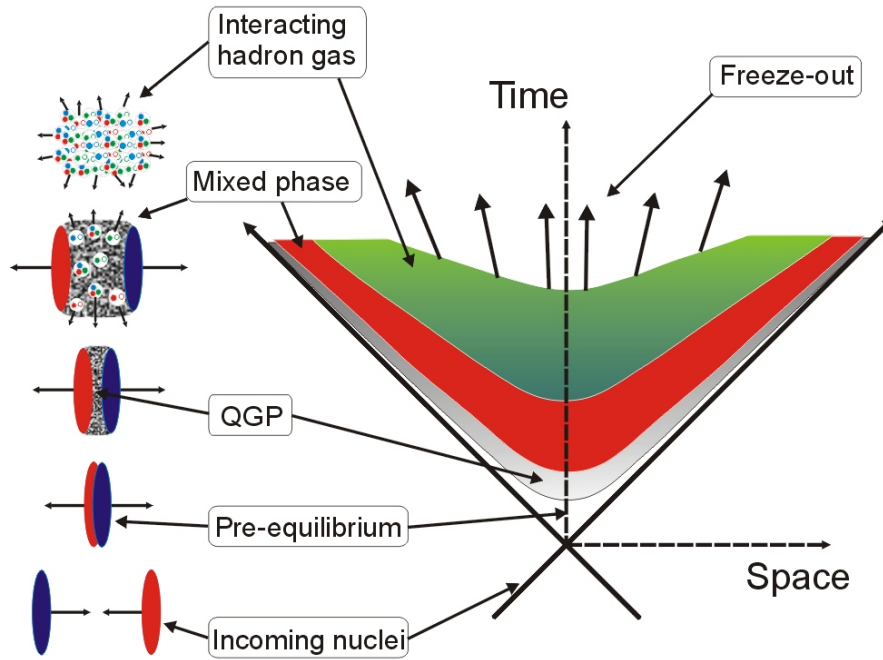
Figure 1.3: Space-time diagram for nucleus-nucleus collision, showing the various stages of the evolution of expanding matter.

leads to an expansion of the system during which its temperature and density are decreasing. If the deconfinement phase transition is of first order the system may go through a *mixed phase* in which the formed hadrons coexist with the deconfined quarks and gluons. Finally, all quarks and gluons condensate into a state of the highly interacting hadron gas which further expands and cools to the point called *chemical freeze-out*, where the last inelastic collisions occur. At this point abundances of all hadrons are fixed and only elastic collisions between particles continue. The final stage where all elastic collisions vanish (*thermal freeze-out*) is reflected in the momenta of the measured particles.

1.2.1 Basics

A particle emitted from an ultrarelativistic nucleus-nucleus collision is commonly described in terms of its transverse momentum $p_\perp$ and the rapidity y. The four-momentum vector p of an emitted particle satisfies the mass-shell constraint $\mathsf{p}^2 = \mathsf{p}^\mu \mathsf{p}_\mu = m^2$ has only three degrees of freedom. In Cartesian coordinates the particle momentum $\vec{\mathsf{p}}$ can be decomposed in the

longitudinal ($p_\parallel$) and the transverse ($p_\perp$) momentum components. The latter is defined as

$$p_\perp = \sqrt{p_x^2 + p_y^2}\,, \tag{1.2}$$

where p_x and p_y are components perpendicular to the beam direction. The $p_\parallel$ component is parallel to the z-axis which coincides with the beam direction. For all presented relations the speed of light c is set to unity. The rapidity variable is defined in terms of the particle energy E and the longitudinal component of the momentum $p_\parallel$

$$y = \frac{1}{2} \ln \left(\frac{E + p_\parallel}{E - p_\parallel} \right) = \ln \left(\frac{E + p_\parallel}{m_\perp} \right), \tag{1.3}$$

where $m_\perp = \sqrt{m^2 + p_\perp^2}$ is the transverse mass with m being the rest mass of particle. In the case of the symmetric system collisions with fixed targets the center-of-mass frame moves with the rapidity $y_{CMS} = 0.5 \cdot y_{beam}$, called therefore mid-rapidity. This leads to the particle rapidity spectrum being symmetric around y_{CMS} and allows to complement the measured particle spectra by reflection. Lorentz transformation between two coordinate frames along the direction of the beam in terms of rapidity has the simple form

$$y_2 = y_1 + y_{12}\,, \tag{1.4}$$

where $y_{12} = \ln \left[\gamma_L \left(1 + \beta_L \right) \right]$ depends on the β_L and γ_L values related to the velocity of the moving frame. It is this simple result which gives the rapidity variable its importance as a tool in the analysis of particle production data. The velocity of the particle is given by

$$\beta = \frac{p}{E} = \sqrt{1 - \frac{1}{\gamma^2}}\,. \tag{1.5}$$

In most experiments angles are measured rather than the three components of $\vec{\mathbf{p}}$. For a particle emitted at a polar angle θ a variable analogous to rapidity, called pseudo-rapidity, can be defined as

$$\eta = -\ln \tan \frac{\theta}{2}\,. \tag{1.6}$$

Since the mass and the momentum do not enter, this observable is easier to determine. It coincides with rapidity at $p_\perp \gg m$. It is useful to rewrite its definition in the form

$$\eta = \frac{1}{2} \ln \left(\frac{p + p_\parallel}{p - p_\parallel} \right) \tag{1.7}$$

which appears to be almost equivalent to Eq. 1.3. Some useful relations, which provide transformation between $(E, p_\perp, p_\parallel)$ and $(m_\perp, y)$, are

$$\begin{aligned}
E &= m_\perp \cosh{(y)}\,, \\
p_\parallel &= m_\perp \sinh{(y)} = E \tanh{(y)} = p \tanh{(\eta)}\,, \\
y &= \tanh^{-1}{(\beta)}\,.
\end{aligned} \tag{1.8}$$

For the two-particle analysis, the main topic of this dissertation, it is useful to define additional variables like the pair four momentum

$$\mathsf{P} = \mathsf{p}_1 + \mathsf{p}_2 \ , \tag{1.9}$$

the pair transverse momentum

$$P_\perp = \sqrt{P_x^2 + P_y^2} \ , \tag{1.10}$$

and the momentum difference

$$\mathsf{q} = \mathsf{p}_2 - \mathsf{p}_1 \ . \tag{1.11}$$

In the pair center-of-mass frame and for particles with the same masses the length of the spatial component of the four-vector q, (q_x, q_y, q_z), becomes equal to the Lorentz invariant four-momentum difference

$$q_{inv} = \sqrt{-\left(\mathsf{q}\right)^2} = \sqrt{-\left((E_2 - E_1)^2 - (\vec{\mathbf{p}_2} - \vec{\mathbf{p}_1})^2\right)} \ . \tag{1.12}$$

1.2.2 Landau Scenario

One of the first description of the space-time evolution of the heavy ion collisions was proposed by Landau in [Lan53]. In this model, the two Lorentz-contracted hadrons or nuclei are completely stopped and the whole energy carried by the participants is transfered into the system with a large energy density (ε) and with the particle production around mid-rapidity. The assumption of the full thermalization of the system in a volume of size $V \approx m_p/\sqrt{E}$, where E is the laboratory energy, justified the use of the classical relativistic hydrodynamics of an ideal (non-viscous and non-heat-conducting) fluid. The energy-momentum tensor $T^{\mu\nu}$ is

$$T^{\mu\nu} = (\varepsilon + p)\,\mathsf{u}^\mu \mathsf{u}^\nu - g^{\mu\nu} p \ , \tag{1.13}$$

where $\mathsf{u}^\mu(x)$ is the four-velocity field with $\mathsf{u}^2 = \mathsf{u}_\mu \mathsf{u}^\mu = 1$ and ε, p are the scalar densities of energy and pressure, respectively. The hydrodynamics equations are given by

$$\partial^\mu T_{\mu\nu} = 0 \ . \tag{1.14}$$

In order to solve these equations an equation of state $\varepsilon = \varepsilon\,(T, p)$ is required. Landau assumption was based on the equation of state describing the non-interacting gas of photons

$$p = \frac{1}{3}\,\varepsilon \tag{1.15}$$

which is characteristic of blackbody radiation. Eqs. 1.14 imply that the initial state entropy, which is produced in the process of thermalization, is distributed in the rapidity space with a

Gaussian form, and the width is determined by the initial Lorentz contraction. In addition, the model assumed that the motion of the ideal fluid has to be adiabatic and thus the entropy of the individual regions of the system remains unchanged during the expansion. A straightforward consequence is the multiplicity formula $N = K E^{1/4}$. The energy density of the created system is given by the energy divided by the volume of the reaction zone. However, in the Landau picture, the volume of the system is known only approximately which leads to a large uncertainty in the estimation of the energy density of created matter. This model should be satisfactory up to AGS collisions energies where the nuclear stopping power is quite large. Above these energies the fraction of the longitudinal energy, which is still present after the collision in the nuclei, is about half of the initial one (transparency of the collisions). Compared to the collisions with full stopping, this inherent longitudinal expansion influences the system's evolution and must be considered in the calculations. Such description of the space-time evolution of the colliding system was proposed by Bjorken [Bjo83] and is discussed in the next section.

1.2.3   Bjorken Scenario

The modification of the initial boundary condition of the Laundau scenario leads to a different particle production distribution and energy density of the colliding system. The Bjorken scenario assumes that at a sufficiently high energy a plateau in the particle production as a function of the rapidity occurs. The rapidity densities dN/dy are assumed to be independent of rapidity for at least a few units of rapidity around mid-rapidity in $p + p$ and $p + A$ collisions from which it is deduced that the same is true for $A + A$ collisions. Thus, this space-time evolution scenario is a boost-invariance model. At high energy heavy ion collisions, like for the SPS energies, the nucleons can still have enough momentum to proceed forward and move away from the collision zone. Transverse expansion of the source can be neglected in the first approximation, because of the large initial transverse scale of the source as compared to its longitudinal scale. This reduces the situation to a two-dimensional problem in the coordinates z and t. Due to the homogeneity of the source in all frames there is no pressure gradient to change the longitudinal flow, and the velocity of each fluid element stays the same. If it is assumed that, at $t = 0$, right after the two nuclei have collided, the longitudinal extent of the source is negligible, the relation $z = \beta t$ therefore holds at all times $t > 0$. The proper time τ is

$$\tau = \sqrt{t^2 \left(1 - \frac{z^2}{t^2}\right)} = \sqrt{t^2 - z^2} = \frac{t}{\gamma} \, , \qquad (1.16)$$

and the z and t variables are related to the space-time rapidity via

$$\begin{aligned} t &= \tau \cosh\left(y\right), \\ z &= \tau \sinh\left(y\right), \end{aligned} \qquad (1.17)$$

with

$$y = \frac{1}{2} \ln\left(\frac{t+z}{t-z}\right) \, . \qquad (1.18)$$

Since the evolution of the system looks the same in all mid-rapidity like frames, the energy density and pressure only depends on τ. This gives rise to hyperbolae of constant energy densities that can be used to distinguish between different phases in the evolution of the collision. The energy density created during collision of nuclei is given by

$$\varepsilon = \frac{\langle E_h \rangle}{\pi R_A^2 \tau_0} \left(\frac{dN_h}{dy} \right)_{y=0} , \tag{1.19}$$

where $\left(\frac{dN_h}{dy} \right)_{y=0}$ is the number of hadrons per unit of rapidity produced at midrapidity, $\langle E_h \rangle$ is the average energy of hadrons, R_A is the nuclear radius, and τ_0 corresponds to the formation time of the medium. The latter was estimated by Bjorken to be $\tau_0 = 1/\Lambda_{QCD} \approx 1$ fm/c.

1.2.4 Observables

The deconfinement state of quarks and gluons is believed to occur above certain temperature or/and density of the matter. During ultra-relativistic heavy ion collisions such hot and dense state of matter can be produced for a time of a few fermi units. This short-live QGP state can only be accessed with probes which will carry the information about it after the system hadronizes. Heavy ion experiments detect mostly the charged hadrons which have lost most of the information about the early stages of the collisions through rescattering and collective expansion. On the other hand, the termalized QGP would emit thermal radiation ($\gamma^* \to e^+e^-$ or $\mu^+\mu^-$) in form of leptons and real photons produced in quark-anti quark annihilation ($q\bar{q} \to \gamma g$) and Compton scattering processes ($qg \to \gamma q$). The photons and leptons interact with matter through the electromagnetic interaction and their mean free path is larger than the size of the system ($\lambda \approx 10^3$ fm). Therefore, they contain information of the system at the time of their emission and transport it almost unaffected to the detectors. Theoretical models expect a shift of the ρ peak to lower masses [BR96] or a broadening and slight shift up [RW00] when ρ is immersed in high density hadronic matter. Such process is attributed to pion annihilation $\pi\pi \to \rho \to e^+e^-$, thus explaining the enhancement observed in the dilepton mass spectrum in heavy ion collisions. The results of a dilepton analysis, performed on the same experimental data set as used for the two-particle correlations analysis discussed in this dissertation, are presented in [MftCC06].

Another observable related to the early stage of the collision is the anisotropic transverse flow. The anisotropic shape of the overlapping nuclei region created in the non-central collisions causes pressure gradient in the system. The almond shape of the overlapping nuclei has its shorter axis in the reaction plane. Therefore, the transverse velocity and the acceleration is larger in-plane than out-of-plane. Thus, the directions of the outgoing particles are correlated to the orientation of the reaction plane. The dependence on the particle emission azimuthal angle, ϕ, measured with respect to the reaction plane orientation, Ψ, can by expressed as Fourier

series [VZ96]

$$E\frac{d^3N}{d^3p} = \frac{1}{2\pi}\frac{d^2N}{p_t dp_t dy}\left(1 + 2\sum_{n\geq 1} v_n \cos(n(\phi - \Psi))\right) \tag{1.20}$$

where $v_n = \langle\cos(n(\phi - \Psi))\rangle$ are the Fourier coefficients. The first two harmonics (n=1,2) describe the directed and the elliptic flow, respectively. Since the flow builds up throughout the evolution of the system, it contains information on both the partonic and the hadronic stage.

Information about the space-time evolution and dynamics of the colliding system accessible through the single momentum spectra and through multiparticle observables are significantly limited in comparison to two-particle momentum distributions. While from the single transverse momentum spectra or from the particle yield analysis the temperature of the freeze-out can be extracted they miss information of the size and the lifetime of the particle emitting source. The only known way to obtain direct experimental information about geometry and dynamics of the reaction zone is through two-particle intensity interferometry. The intensity interferometry provids crucial information for an assessment of theoretical models which try to extract the energy densities of the source from the measured single particle spectra and particle multiplicity density in momentum space. Reliable estimates of the source volume and the energy density are, on the other hand, indispensable for an experimental proof that high energy collisions can successfully generate large volumes of matter with extreme energy density, where a transition into deconfined quark matter might be possible. Therefore, a systematic analysis of the two-particle correlations are of great importance in the search of the QGP. The detailed information concerning the two-particle analysis are presented in following sections as it is the main topic of this dissertation.

1.3   Two-particle Interferometry

The technique of intensity interferometry was introduced by Hanbury-Brown and Twiss to measure angular dimensions of stars [HBT56] and it is after them that this technique is called **HBT**. In the sixties this technique was independently discovered and applied to the subatomic physics as a tool to investigate the space-time evolution of the elementary-particle and nuclear collisions. In the original astrophysics applications of the technique the source was a distant radio-wave emitter while in applications involving the collision of nuclei or particles the source is the reaction region. Experimentally, particles interferometry was first used by Goldhaber, Goldhaber, Lee, and Pais ($GGLP$) [GGLP60] to determine the dimensions of the pion production region in $p\bar{p}$ annihilation. They suggested that the observed enhancement of closes pairs of identical pions is a consequence of the Bose-Einstein symmetrization. The interpretation of pion emission in terms of intensity interferometry was pursued more then a decade later by Shuryak [Shu73]. Kopylov and Podgoretskii expressed the HBT effect in terms of the two-particle correlation functions [KP71] and settled the basis of the technique in nuclear

collisions.

In contrast to the conventional amplitude interferometry, where the interference pattern is observed when coherent particles pass through slits, in the intensity interferometry a correlation function $(C_2 = (\langle n_{12} \rangle / \langle n_1 \rangle \langle n_2 \rangle) - 1)$ is constructed from the number of counts n_1 and n_2 measured at positions D1 and D2. In Fig. 1.4 the schematic representation of the emissions of two indistinguishable particles observed in detectors is shown. The correlation function is proportional to the intensity of the particle pairs arriving at D1 and D2. The fact that the identical particles cannot be distinguish between themselves imply that the origin of the observed particle correlations is the symmetry (anti-symmetry) of the quantum mechanical wave functions of identical bosons (fermions).
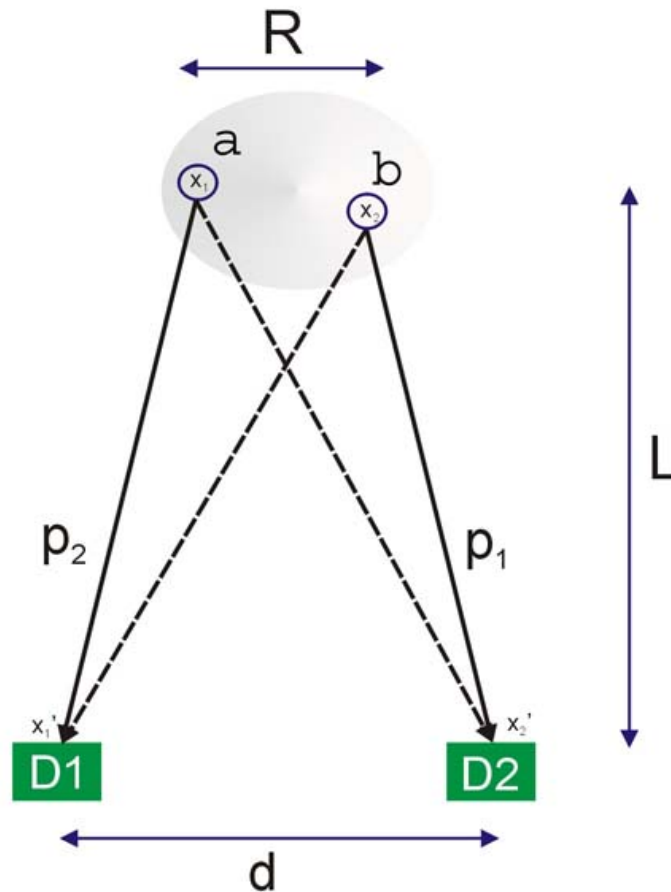
Figure 1.4: Measurement of the separation of two sources, a and b, by correlations of intensities in detectors D1 and D2. L is the distance between an emitting source and detectors, and d is the separation between detectors.

1.3.1   Correlation Function and Source Function

The simplest picture of HBT interferometry, from which it is possible to deduce the fundamental idea, is to consider two distant random points sources of particles, x_1 and x_2, within some generalized source, and a pair of detectors D1 and D2 placed at x'_1 and x'_2, respectively, as depicted in Fig. 1.4. The emitted particles can be represented by plane waves which must be symmetrized (antisymmetrized) according to the Bose-Einstein (Fermi-Dirac) statistics present

$$\Psi = \frac{1}{\sqrt{2}} \left[e^{i\left(x'_1 - x_1\right)p_1} e^{i\left(x'_2 - x_2\right)p_2} \pm e^{i\left(x'_1 - x_2\right)p_1} e^{i\left(x'_2 - x_1\right)p_2} \right] \ . \tag{1.21}$$

The two measured momenta are denoted as p_1 and p_2. The probability density of a system of two identical bosons is then given by the square of the plane wave function

$$|\Psi_{1,2}|^2 = |\Psi_{2,1}|^2 = 1 + \cos\left[(p_2 - p_1) \cdot (r_2 - r_1)\right] \ . \tag{1.22}$$

Then the probability of measuring two particles with momenta p_1 and p_2 in the detectors is given by the integration of the probability density $|\Psi_{1,2}|^2$ over the emission function $S(x, p)$,

$$P(\mathbf{p_1}, \mathbf{p_2}) = \int S(x_1, p_1) S(x_2, p_2) |\Psi_{1,2}|^2 d^4x_1 d^4x_2 \ , \tag{1.23}$$

while the single particle probability is expressed by

$$P(\mathbf{p}) = \int S(x, p) \ d^4x \ . \tag{1.24}$$

Introducing Eq. 1.21 in Eq. 1.23 and assuming that the emission function has a smooth momentum dependence, the two-particle probability can be expressed as

$$\begin{aligned} P(\mathbf{p_1}, \mathbf{p_2}) = &\ P(\mathbf{p_1}) P(\mathbf{p_2}) \\ &\pm \int d^4x \cos(q \cdot r) \cdot \int S\left(R + \frac{X}{2}, k\right) S\left(R - \frac{X}{2}, k\right) d^4X \ , \end{aligned} \tag{1.25}$$

where $R = x_2 - x_1$, $X = \frac{1}{2}(x_1 + x_2)$, r is relative separation and last term corresponds to the relative distance distribution [WH99]. The correlation function is defined as the two-particle probability (1.24) normalized to the products of single particle probabilities and is equal to

$$C(\mathbf{q}, \mathbf{P}) \approx 1 \pm \frac{|\int d^4x \, S(x, P) \, \exp(iq \cdot x)|^2}{|\int d^4x \, S(x, P)|^2} \ . \tag{1.26}$$

The expression takes the plus sign for boson pairs and the minus sign for fermion pairs. The source function $S(x, P)$ in Eq. 1.26 describes the single particle densities at freeze-out. The source function can be identified with the Wigner transform of the density matrix associated with the classical source amplitudes [Hei96a]. This Wigner density is a quantum mechanical

object defined in phase-space of **x** and **P**. The integration over phase-space leads to the classical source density in momentum or coordinate space and provides the probability of finding at space-time point **x** a source which emits a particle with momentum **P**. The simplest approximation of the emission source model is given by space-time Gaussians in its center-of-mass frame

$$S(\mathsf{x}, \mathsf{P}) = f(\mathsf{P}) \exp\left[-\frac{x^2 + y^2}{2R_\perp^2} - \frac{z^2}{2R_\parallel^2} - \frac{(t - t_0)^2}{2(\Delta t)^2} \right] . \tag{1.27}$$

The overview of the different source models can be found in [CNH95].

The space-time saddle point $\bar{\mathsf{x}}(\mathsf{P})$ of the emission function $S(\mathsf{x}, \mathsf{P})$ is defined via four equations [AS95]

$$\left. \frac{\partial}{\partial \mathsf{x}_\mu} \ln(S(\mathsf{x}, \mathsf{P})) \right|_{\bar{\mathsf{x}}} = 0 , \tag{1.28}$$

where $\mu = \{0, 1, 2, 3\}$. The saddle point is a point in space-time which has the maximum probability of emitting a particle with momentum **P**.

The correlation function between two identical bosons is sensitive to the following physical quantities

- the geometrical extension of the collision region at the time of last hadronic scattering (freeze-out),

- the freeze-out time and particle emission duration,

- the collective velocity of the expanding collision region in the direction parallel and perpendicular to the beam,

- the azimuthal asymmetry of the particle source in collisions with a finite impact parameter collisions.

The experimantal two-particle correlation function is constructed from the single- and two-particle cross sections

$$C(\mathbf{p}_1, \mathbf{p}_2) = \sigma_0 \frac{\frac{d^3\sigma}{d^3p_1 d^3p_2}}{\frac{d^3\sigma}{d^3p_1} \frac{d^3\sigma}{d^3p_2}} . \tag{1.29}$$

The detailes of the procedure are explained in Section 5.2.

1.3.2 Coordinate Systems and Variables

The widely used Gaussian parameterization of the experimental two-particle correlation functions provides a relationship of the corresponding width parameters (HBT radii) with the space-time structure of the source. This relation is based on a quadratic saddle-point approximation

to the true space-time dependence of the emission function and yields

$$S(\mathsf{x},\mathsf{P}) \approx S(\bar{\mathsf{x}}(\mathbf{P}),\mathsf{P}) \exp\left[-\frac{1}{2}\left(\mathsf{x}-\bar{\mathsf{x}}(\mathbf{P})\right)^\mu B_{\mu\nu}(\mathbf{P})\left(\mathsf{x}-\bar{\mathsf{x}}(\mathbf{P})\right)^\nu\right],\qquad(1.30)$$

where the symmetric curvature tensor $B_{\mu\nu}$ is given by

$$B_{\mu\nu}(\mathbf{P}) = \left. -\partial_\mu\partial_\nu \ln\left(S\left(x,P\right)\right)\right|_{\bar{x}}.\qquad(1.31)$$

The latter contains, in general, ten independent components, however, only six **P**-dependent parameters can be measured by making a Gaussian fit in q to the measured correlation function, due to the on-shell constraint.

Introducing the following notation of the **P**-dependent average of an arbitrary space-time function $\xi(\mathsf{x})$ [CSH95] with the source density $S(\mathsf{x},\mathsf{P})$

$$\langle\xi\rangle \equiv \langle\xi(\mathsf{x})\rangle(\mathbf{P}) = \frac{\int d^4\mathsf{x}\,\xi(\mathsf{x})\,S(\mathsf{x},\mathsf{P})}{\int d^4\mathsf{x}\,S(\mathsf{x},\mathsf{P})}\qquad(1.32)$$

it is possible to express the correlation function Eq. 1.26 in form

$$C(\mathbf{q},\mathbf{P}) \approx 1 \pm \left|\langle\exp\left(i\mathbf{q}\cdot\mathsf{x}\right)\rangle(\mathbf{P})\right|^2.\qquad(1.33)$$

The space-time coordinates $(\mathsf{x}-\bar{\mathsf{x}}(\mathbf{P}))^\mu$ in Eq. 1.30 are defined relative to the "effective source center" $\bar{\mathsf{x}}(\mathbf{P})$ for bosons emitted with momentum **P**. Furthermore, within the saddle-point approximation Eq. 1.30, the following relations hold

$$\langle\mathsf{x}_\mu\rangle = \bar{\mathsf{x}}_\mu(\mathbf{P}),\qquad(1.34)$$

$$\left(B^{-1}\right)_{\mu\nu}(\mathbf{P}) = \langle\mathsf{x}_\mu\mathsf{x}_\nu\rangle - \langle\mathsf{x}_\mu\rangle\langle\mathsf{x}_\nu\rangle.\qquad(1.35)$$

The saddle point is thus the average space-time point from which particle pairs with momentum **P** are emitted, and the component of the inverse of the curvature tensor $\left(B^{-1}\right)_{\mu\nu}(\mathbf{P})$ gives the space-time correlations of the source. The four diagonal elements

$$\left(B^{-1}\right)_{\mu\mu}(\mathbf{P}) = \left\langle\mathsf{x}_\mu^2\right\rangle - \left\langle\mathsf{x}_\mu\right\rangle^2\qquad(1.36)$$

can be understood as the squares of the "lengths of homogeneity" of the source as seen by the pairs with momentum **P** [AS95]. Based on the approximations of Eq. 1.26 and Eq. 1.30 the Gaussian form of the correlation function can be written as

$$C(\mathbf{q},\mathbf{P}) = 1 \pm \exp\left[-\mathsf{q}^\mu\mathsf{q}^\nu\left(B^{-1}\right)_{\mu\nu}(\mathbf{P})\right].\qquad(1.37)$$

This involves the smoothness and on-shell approximations which permit to write the space-time variances $\left(B^{-1}\right)_{\mu\nu}(\mathbf{P})$ as a function of **P** only. Different Gaussian parameterizations of Eq. 1.37

exist depending of the choice of the three independent components, the fourth component of $\mathbf{q}$ in Eq. 1.11 is fixed by the requirement that the final state particles are on-shell

$$\mathsf{q} \cdot \mathsf{P} = (\mathsf{p}_2^2 - \mathsf{p}_1^2) = 0 \Rightarrow q_0 = \frac{\mathbf{P} \cdot \mathbf{q}}{P_0} \,, \tag{1.38}$$

and thus cannot be studied independently of the other three. The Cartesian parameterization proposed by G.Bertsch and S.Pratt [Ber89, Pra86b] is based on an elimination of the temporal component from Eq. 1.37 via the mass-shell constraint, $q^0 = \beta_\perp q_{out} + \beta_{long} q_{long}$, with $\beta_\perp = |P_\perp/P^0|$ being the velocity of the particle pair transverse to the beam direction while β_{long} is its longitudinal component. The decomposition of the relative momentum three-vector $\overrightarrow{\mathbf{q}}$ in the "out-side-long" coordinate system is shown in Fig. 1.5. Therefore, Eq. 1.37 can be expressed by the relation

$$C\left(\mathbf{q}, \mathbf{P}\right) = 1 \pm \exp\left[- \sum_{i,j=out,side,long} R_{ij}^2(\mathbf{P})\, \mathsf{q}^i \mathsf{q}^j \right] \,, \tag{1.39}$$

where the six HBT "radius parameters" $R_{ij}^2(\mathbf{P})$ are given as [CSH95, HB95]

$$R_{ij}^2\left(\mathbf{P}\right) = \left\langle \left((\mathsf{x} - \bar{\mathsf{x}}(\mathbf{P}))_i - \beta_i \hat{t} \right) \left((\mathsf{x} - \bar{\mathsf{x}}(\mathbf{P}))_j - \beta_j \hat{t} \right) \right\rangle, \quad i,j = out, side, long, \tag{1.40}$$

through the space-time variances of the source function. In general the correlation function $C\left(\mathbf{q}, \mathbf{P}\right)$ depends not only on $P_\perp$ and P_{long} but also on the azimuthal orientation Ψ of the
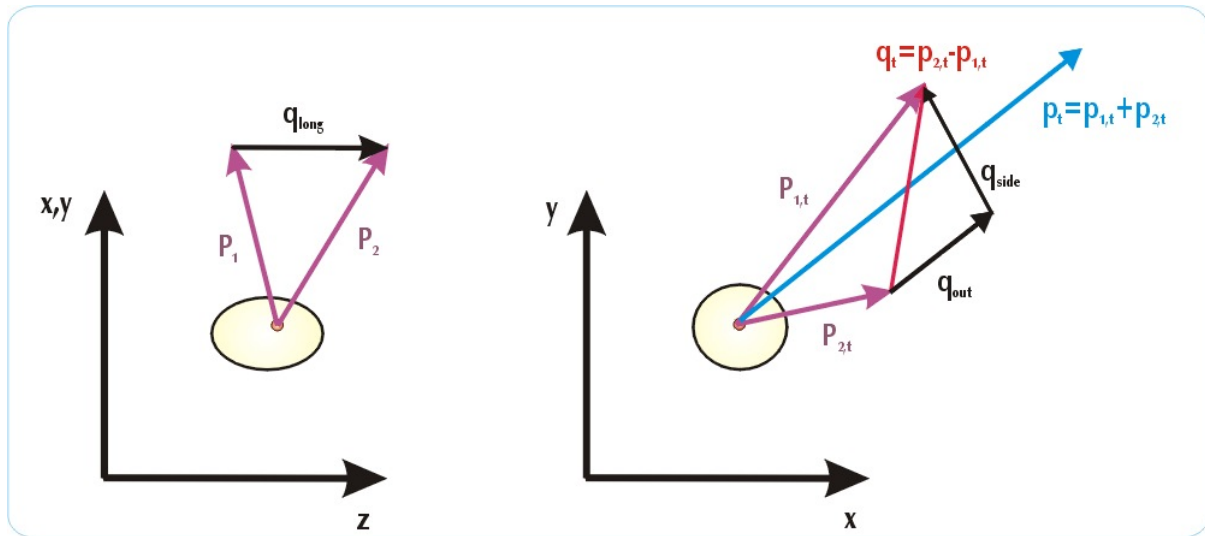
Figure 1.5: The "out-side-long" coordinate system takes the longitudinal "long" direction along the beam axis. In the transverse plane, the "out" direction is chosen parallel to the transverse component of the pair momentum $P_\perp$ defined as Eq. 1.10, and the "side" direction is perpendicular to the "out" vector.

transverse pair momentum with respect to some pair-independent direction in the laboratory system, e.g. relative to the impact parameter $\overrightarrow{b}$.

In the case of the central collisions $|\overrightarrow{b}| \rightarrow 0$ the collision region is azimuthally symmetric and the emission function and the $C(\mathbf{q}, \mathbf{P})$ are Ψ-independent. For such a collision the $R_{out,side}^2$ and $R_{out,side}^2$ parameters in Eq. 1.39 vanish and only four independent HBT "radius parameters" remain. Defining $\tilde{x} = \mathsf{x} - \bar{\mathsf{y}}(\mathbf{P})$ it is possible to express the non-vanishing HBT-radius parameters by [CSH95]

$$R_s^2(\mathbf{P}) = \left\langle \tilde{y}^2 \right\rangle (\mathbf{P}) , \tag{1.41}$$

$$R_o^2(\mathbf{P}) = \left\langle \left(\tilde{x} - \beta_\perp \tilde{t} \right)^2 \right\rangle (\mathbf{P}) , \tag{1.42}$$

$$R_l^2(\mathbf{P}) = \left\langle \left(\tilde{z} - \beta_\| \tilde{t} \right)^2 \right\rangle (\mathbf{P}) , \tag{1.43}$$

$$R_{ol}^2(\mathbf{P}) = \left\langle \left(\tilde{x} - \beta_\perp \tilde{t} \right) \left(\tilde{z} - \beta_\| \tilde{t} \right) \right\rangle (\mathbf{P}) . \tag{1.44}$$

Another symmetry that may apply to the emission function, is the longitudinal boost-invariance (Bjorken expansion). For such model, near the mid-rapidity, the longitudinal boost-invariance implies a $\tilde{z} \rightarrow -\tilde{z}$, thus in additional to the space-time variances linear in $\tilde{y}$, now also those linear in $\tilde{z}$ vanish. In the longitudinally comoving system (LCMS), where $\beta_\| = 0$, this leads to further simplification

$$R_l^2(\mathbf{P}) = \left\langle (\tilde{z})^2 \right\rangle (\mathbf{P}) , \tag{1.45}$$

$$R_{ol}^2(\mathbf{P}) = 0 . \tag{1.46}$$

However, if the azimuthal symmetry of the particle emitting source is broken, then the single particles transverse momentum spectrum depends on the azimuthal direction of the emitted particles. This implies that the two-particles correlation functions should, in general, depend on azimuthal direction Ψ of the pair momentum, as well [VC96, Wie98]. The corresponding Gaussian radius parameters can be written formally in terms of space-time variances which are rotated via $\mathcal{D}_\Psi$ (see Eq. 2.2a in [Wie98]) from the impact parameter fixed to the $out-side-long$ coordinate system

$$R_{ij}^2(\mathbf{P}) = \left\langle \left((\mathcal{D}_\Psi \tilde{x})_i - (\mathcal{D}_\Psi \beta)_i \tilde{t} \right) \left((\mathcal{D}_\Psi \tilde{x})_j - (\mathcal{D}_\Psi \beta)_j \tilde{t} \right) \right\rangle ,$$
$$(\mathcal{D}_\Psi \beta) = \left(\beta_{\perp,0,\beta_\|} \right) . \tag{1.47}$$

The x, y and z are here given in the impact-parameter fixed system, not the $out-side-long$ one. As for the azimuthally symmetric case, the HBT radius parameters show implicit and explicit $\mathbf{P}$-dependences

$$R_s^2(P_\perp, \Psi, Y) = \left\langle \tilde{x}^2 \right\rangle \sin^2 \Psi + \left\langle \tilde{y}^2 \right\rangle \cos^2 \Psi - \langle \tilde{x}\tilde{y} \rangle \sin 2\Psi ,$$

$$R_o^2\left(P_\perp, \Psi, Y\right) = \left\langle \tilde{x}^2 \right\rangle \cos^2 \Psi + \left\langle \tilde{y}^2 \right\rangle \sin^2 \Psi + \beta_\perp^2 \left\langle \tilde{t}^2 \right\rangle$$
$$- 2\beta_\perp \left\langle \tilde{t}\tilde{x} \right\rangle \cos \Psi - 2\beta_\perp \left\langle \tilde{t}\tilde{y} \right\rangle \sin \Psi + \left\langle \tilde{x}\tilde{y} \right\rangle \sin 2\Psi \,,$$
$$R_l^2\left(P_\perp, \Psi, Y\right) = \left\langle \left(\tilde{z} - \beta_\parallel \tilde{t}\right)^2 \right\rangle \,,$$
$$R_{os}^2\left(P_\perp, \Psi, Y\right) = \left\langle \tilde{x}\tilde{y} \right\rangle \sin 2\Psi + \frac{1}{2} \sin 2\Psi \left(\left\langle \tilde{y}^2 \right\rangle - \left\langle \tilde{x}^2 \right\rangle\right)$$
$$+ \beta_\perp \left\langle \tilde{t}\tilde{x} \right\rangle \sin \Psi - \beta_\perp \left\langle \tilde{t}\tilde{y} \right\rangle \cos \Psi \,,$$
$$R_{ol}^2\left(P_\perp, \Psi, Y\right) = \left\langle \left(\tilde{z} - \beta_\parallel \tilde{t}\right)\left(\tilde{x} \cos \Psi + \tilde{y} \sin \Psi - \beta_\perp \tilde{t}\right) \right\rangle \,,$$
$$R_{sl}^2\left(P_\perp, \Psi, Y\right) = \left\langle \left(\tilde{z} - \beta_\parallel \tilde{t}\right)\left(\tilde{y} \cos \Psi - \tilde{x} \sin \Psi\right) \right\rangle \,. \tag{1.48}$$

The explicit Ψ-dependence is a purely geometrical consequence of rotating the x-axis from the direction of $\vec{b}$ to the direction of $P_\perp$.

1.3.3 Final State Interactions Between Particles

For pairs of identical bosons (fermions) the two-particle wave function describing their propagation towards the detector must be symmetrized (antisymmetrized). For boson pairs this results in quantum statistical "Bose-Einstein correlations" between the final state momenta of the two particles. Via the uncertainty relation these momentum space correlations reflect the spatial and temporal structure of the source from which the two particles were emitted. This correspondence forms the basis for Bose-Einstein interferometry in nuclear and particle physics considered in previous sections. In addition to the Bose-Einstein and the Fermi-Dirac effects, the particles, which leave the interaction region, may be subject to mutual strong or Coulomb final state interaction (FSI) and thus cannot be described by plane waves. In the case of charged particles, the mutual Coulomb interaction leads to an enhancement or a suppression of the measured correlation function at small q for unlike-sign and like-sign pairs, respectively. In Section 1.3.4 it is shown that the FSI between different particles species offer supplementary information about properties of the emitting source created in a collisions of heavy ions. The strong FSI through resonances has been discussed based on the wave function formalism, the string model, and within the Wigner function formalism [Wei00]. The two most important effects of hadron resonances are the increase of correlation radius and the lowering of the correlation intercept because of short- and long-lived resonances, respectively. Concerning the strong interactions between pions within a pair it has been argued [Bow88] that the range of strong interactions is smaller (~0.2 fm) than the size of the hadronic source and therefore the correlation should be essentially unaffected. The expected source size in the Pb-Au collisions at 158 AGeV is about 6 fm and consequently effects of strong interaction are neglected in this dissertation.

The Coulomb interaction between two particles was considered classically in [BBM96].

Particles of the same (opposite) charge are pushed away from (towards) each other, thus depressing (enhancing) the observed distribution of pairs at small q. The Coulomb interaction with the rest of the fireball, on the other hand, was shown to be less important. Better insight into the Coulomb induced correlations and, especially, their dependence on the source size, is achieved within the non-relativistic quantum mechanical approach. By reversing the time the particle emission is transformed to particle scattering. By introducing the reduced mass

$$\mu = \frac{m_1 \, m_2}{m_1 + m_2} \; . \tag{1.49}$$

the relative motion of the two particles is replaced by a single particle moving in the Coulomb field of the other. The seeked Coulomb factor is then equal to the square of the wave function. The Schrödinger equation for the Coulomb wave function reads

$$\left[-\frac{\nabla^2}{2\mu} + V\left(\vec{r_2} - \vec{r_1}\right) \right] \Psi_{coul}\left(\vec{k}, \vec{r}\right) = E_p \Psi_{coul}\left(\vec{k}, \vec{r}\right) \; , \tag{1.50}$$

where E_p is the energy of the pair, $V\left(\vec{r_2} - \vec{r_1}\right)$ the Coulomb potential energy, and μ the reduced mass. The general solution of Eq. 1.50 is written in terms of the confluent hypergeometric function F [Mer61, Pra86a]. The wave function Ψ_{coul} squared is

$$\left[\Psi_{coul}\left(\vec{k}, \vec{r}\right)\right]^2 = H\left(\vec{k}, \vec{r}\right) = G(\eta) \left| e^{i\left(\vec{r} \cdot \vec{k}\right)} F\left(-i\eta; 1; ik\left(r - \frac{\vec{r} \cdot \vec{k}}{k}\right)\right) \right|^2 \; , \tag{1.51}$$

where $\vec{k}$ is the asymptotic momentum of a particle in the pair center-of-mass system equal to $\frac{q_{inv}}{2}$. In the limit of the point-like source, $\left(\vec{r_2} - \vec{r_1}\right) \to 0$, the squared amplitude of the Coulomb wave function reduces to the classical Gamow function [GKW79]

$$G(\eta) = \frac{2\pi\eta}{e^{2\pi\eta} - 1} = |\Gamma(1 + i\eta)|^2 \exp(-\pi\eta) \; . \tag{1.52}$$

The relative velocity enters through $\eta = 2 \, Z_1 Z_2 \, \mu \, \alpha / q_{inv}$, called Sommerfeld parameter, where α is the fine structure constant and $Z_1 Z_2$ is the product of charges. The Coulomb correlation function is then [Bay98]

$$\frac{C_2^{exp}}{C_2^0} = \int d^3r \, \rho(\vec{r}) \, H\left(\vec{k}, \vec{r}\right) \; , \tag{1.53}$$

where $\rho(\vec{r})$ is the source function which describes the probability of emitting a pair of particles with momentum k at relative distance r, and C_2^0 denotes the correlation function in absence of Coulomb field. For actual calculation usually a spherical Gaussian source is used, $\rho(\vec{r}) = \frac{1}{\sqrt{2\pi}^3 R^3} \exp(-\vec{r}^2/2R^2)$. Since $\vec{r}$ represents the relative distance between the two particles a realistic R should be $\sqrt{2}$ times larger than the experimental HBT radius. The Coulomb wave function squared averaged over a spherical Gaussian source is called $F_c\left(q_{inv}\right)$ and in absence of other sources of correlations may be directly compared to the experimental correlation function.

Apart from the Coulomb interaction between particles in the pair, particles feel the attractive or repulsive interaction, depending on their charge, caused by the positively charged fireball. However, the impact of this effect on the measured $\pi - \pi$ correlation functions was found to be insignificant [ZBB$^+$84, Bar99]. The two-particle correlation functions discussed in this work are not corrected for it.

1.3.4 Non-identical Particle Correlations

Correlation functions of non-identical particles contain information on the relative space-time asymmetries in particle emission [LLEN96]. The ones generated mostly by the Coulomb interaction have an exponential-like shape at **q**=0. The width depends on the average distance squared between the particles at freeze-out, similarly as in the case of identical particle correlations. As was pointed out in [RL04], flow induces a correlation between particles velocities and emission points leading to an effective decrease of measured HBT radii and to different average emission points for particle species with different masses. From this point of view, non-identical correlation can be used as an independent method of flow measurement in heavy ion collisions. The pioneering experimental data analysis of the relative space-time asymmetries in particle emission is presented in [Miś98]. For non-identical particles the generalized momentum difference is defined as

$$\tilde{\mathbf{q}} = \mathbf{q} - \mathbf{P}(\mathbf{qP})/\mathbf{P}^2 \,, \tag{1.54}$$

where **q** is defined by Eq. 1.11, **P** is defined by Eq. 1.10, and $\mathbf{qP}=m_1^2 - m_2^2$. In Fig. 1.6 a simple presentation of the asymmetry mechanism is shown. The origin of the correlation function asymmetry in pion-proton correlations can be understand using this simple sketch. In order to construct correlation function for pair of particles with the different masses one need to select the fast heavier particle while the lighter should be slow one. Thus one can distinguish two scenarios of the particle correlations, namely, in the first case pions tend to catch up with
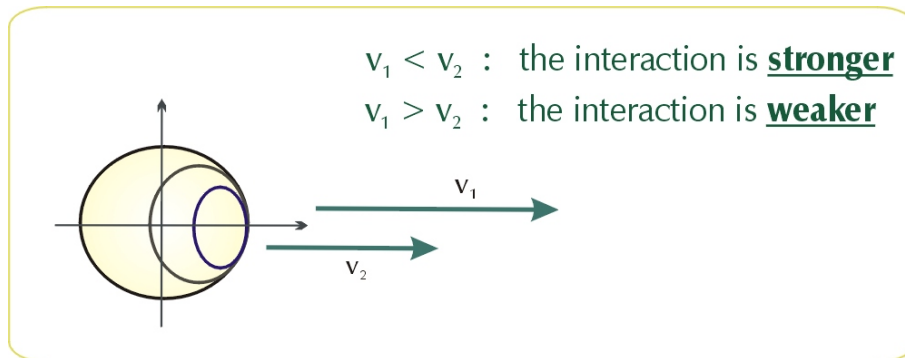
Figure 1.6: The origin of the asymmetry in a non-identical particle correlation function.

protons while in the second case pions tend to move away from protons. The correlations will be stronger in the first case then in the second one, due to longer interaction time between the particles.

Chapter 2

CERES experiment

The CERES (Cherenkov Ring Electron Spectrometer) experiment was operated at the CERN SPS facility and focused on measurement of low-mass e^+e^- pairs emitted in proton- and ion-induced collisions at ultra-relativistic energies. Dileptons and photons are especially attractive probes of QGP since they are produced at all stages of the collision and, in contrast to hadrons, interact mostly electromagnetically. Therefore, they can probe directly the early stage of the collision and carry this information to the detectors. The low-mass dilepton region is governed by the light quark flavors - u, d, and s. In the limit of vanishing quark masses the QCD phase transition is associated with the chiral symmetry restoration which should be manifested in medium modification of the light vector mesons (ρ, ω, ϕ). Here, the ρ meson is of a particular interest because of its short lifetime (τ= 1.3 fm/c) in comparison to the lifetime of the fireball (τ=10-50 fm/c). Low mass lepton pairs are produced only with a 10^{-5} fraction relative to pions. The Cherenkov threshold in the RICH (Ring Imaging Cherenkov) detectors was chosen such to distinguish electrons from other charged particles. The material budget used to construct the detector was kept low to minimize the conversion of photons into the secondary e^+e^- pairs.

The spectrometer covers pseudo-rapidity region $2.1 < \eta < 2.65$ and full azimuthal acceptance as well as very broad range of transverse momentum ($p_\perp$). The initial experimental setup consisted of two RICH detectors providing the electron identification and the measurement of the particle trajectory. The superconducting magnet placed between the RICHes provided an azimuthal symmetric magnetic field. The information about particle charge and momentum was obtained from the deflection angle in the magnetic field between the two RICH detectors. With this configuration different measurements were performed [A$^+$95, A$^+$98b, A$^+$98a]. In order to cope with the high multiplicity environment encountered in collisions induced by lead ions the experimental setup was extended in 1994-95 by two Silicon Drift Counters (SDD) for the vertex reconstruction, the measurement of the energy loss (dE/dx), and coordinates of charged particle tracks with high spatial resolution. In addition, the Multi-Wire Proportional Chamber (MWPC) with a pad readout was located behind the RICH2 mirror. The pad chamber provided an external tracking behind the magnetic field [H$^+$ 1] and facilitated the ring

21

recognition in the RICH2 detector. In 1998, the pad chamber was replaced by the cylindrical Time Projection Chamber (TPC) with radial drift field to enhance the mass resolution for the light vector mesons ρ/ω and ϕ up to $\delta m/m = 2\%$ at $m \approx 1$ GeV/c^2. The TPC also extended the experiment's capability to measure the hadronic signatures of the hot and dense matter. The whole CERES experimental setup enabled the exploration of charged particles only. The neutral particles could be accessed by probing the charged products from their decays.
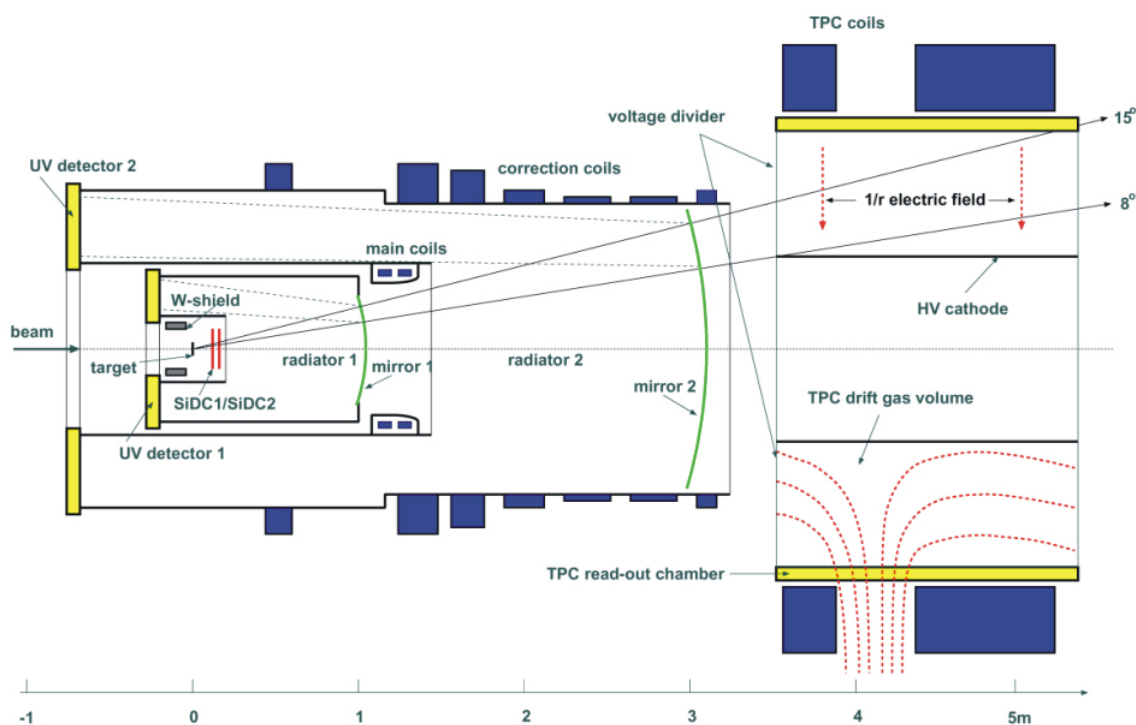
Figure 2.1: CERES experiment setup used for the measurement of Pb-Au collisions in 2000.

In Fig. 2.1 the schematic view of the experimental setup is presented. In 2000 about 33 million Pb-Au collision events at the top SPS beam energy were recorded with this setup. The results presented in this thesis were obtained from analysis of this data set. The CERES experiment was decommissioned in the fall 2003.

2.1   Target and Trigger Systems

During the beam-time in the year 2000 the target system consisted of 13 gold discs of 600 μm diameter and 25 μm thickness. The distance between the discs was chosen to be 1.98 mm to
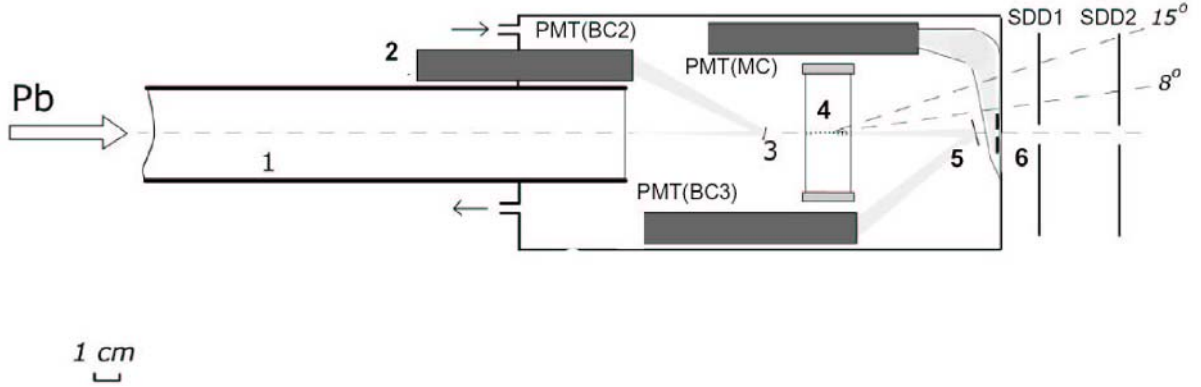
Figure 2.2: The target system together with Silicon Drift Detectors and part of the trigger system: 1) carbon vacuum beam pipe, 2) PMT housing (BC2), 3) BC2 mirror, 4) 13 Au targets, 5) BC3 mirror, 6) multiplicity counter.

minimize the conversion of γ's into e^+e^--pairs and the probability of the secondary interaction. The target region and a part of the trigger system are shown in Fig. 2.2. The target is surrounded by a tungsten shield to absorb charged particles scattered backwards which might otherwise hit the RICH UV-detector.

The trigger system was based on gas Cherenkov counters BC1, BC2 and BC3 and scintillator counters MC, MD and Veto. Each gas Cherenkov counter was composed of the 12 μm aluminum-mylar mirror and the photomultiplier (PMT). The Multiplicity Counter (MC) was a plastic scintillator covering $2.3 < \eta < 3.5$ located 79 mm behind the target with reference to its centre. The schematic view of the trigger and silicon drift detectors is shown in Fig. 2.3 (the Veto wall is not shown). Combination of signals from the beam counters was used to define a collision. The logical expression used for triggering on nuclear interactions, called *minimum bias* (mb), is given by

$$T_{mb} = BC1 \times BC2 \times \overline{BC3} \tag{2.1}$$

The direct measurement of the impact parameter is not possible in the experiments. However, based on assumption that collisions with smaller impact parameter will produce more particles, one can use charged particle multiplicity to extract the impact parameter and classify an event. The centrality selection was based on the MC scintillator with the signal proportional to the number of charged particles. The centrality trigger was defined as

$$T_{central} = T_{mb} \times MC \tag{2.2}$$

The MC threshold was set to trigger on the most central collisions of 7% of the geometrical cross section (σ/σ_{geo}). A fraction of the data (3 M) was taken with $\sigma/\sigma_{geo} = 20\%$ and about (0.5 M) of the minimum bias. For further information about implementation of the trigger system we refer to [Miś99].
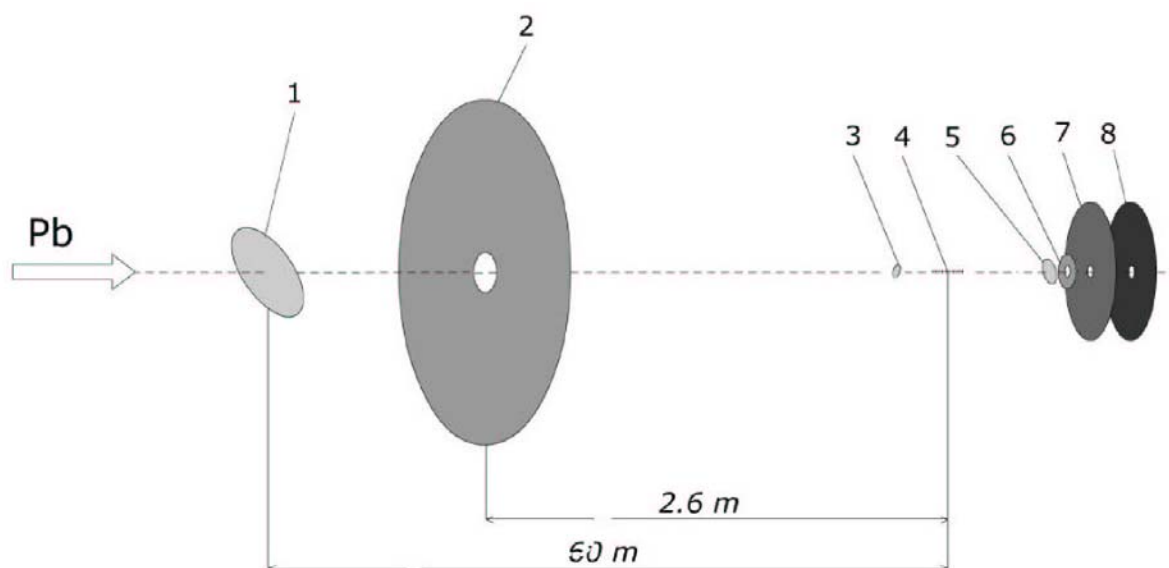
Figure 2.3: The layout of the trigger and the drift detectors: 1) BC1 mirror, 2) veto scintillator (VC), 3) BC2 mirror, 4) 13 Au targets, 5) BC3 mirror, 6) multiplicity counter (MC), 7,8) silicon drift detectors (SDD).

2.2   Silicon Drift Detectors

The determination of the interaction point was based on the two drift silicon detectors (SDD1, SDD2), being located downstream from the target approx. 10 and 14 cm, respectively, as shown in Fig. 2.2. Both detectors are 4 inch silicon wafers covering the full azimuthal acceptance and the pseudo-rapidity region $1.6 < \eta < 3.4$. The thickness of each silicon wafer was 280 μm.

The working principle of the SDD is shown in Fig. 2.4 [GR84]. The charged particle passing through the silicon wafers creates electron-hole pairs along its trajectory. The drift field created by the field rings of the voltage divider transports the freed electrons towards the outside edge of the silicon wafers were the anode pads are located, while the holes are attracted by the nearest strip of the voltage divider. The shape of the drift field is an asymmetric parabola in the beam direction, this peculiar shape resulting in an uniform detector response. The maximum drift time for a drift field of 700 V/m is approx. 3.8 μs. Based on the drift time information it is possible to reconstruct the hit position in the radial direction. The readout electronics channels were connected to the 360 anodes radially arranged at the edges of the SDD detectors. The shape of the anode pad is shown in Fig. 2.5. The segmented structure improves the azimuthal resolution by charge sharing between the anodes.

Additionally the silicon drift detectors were used to determine the charged particle density
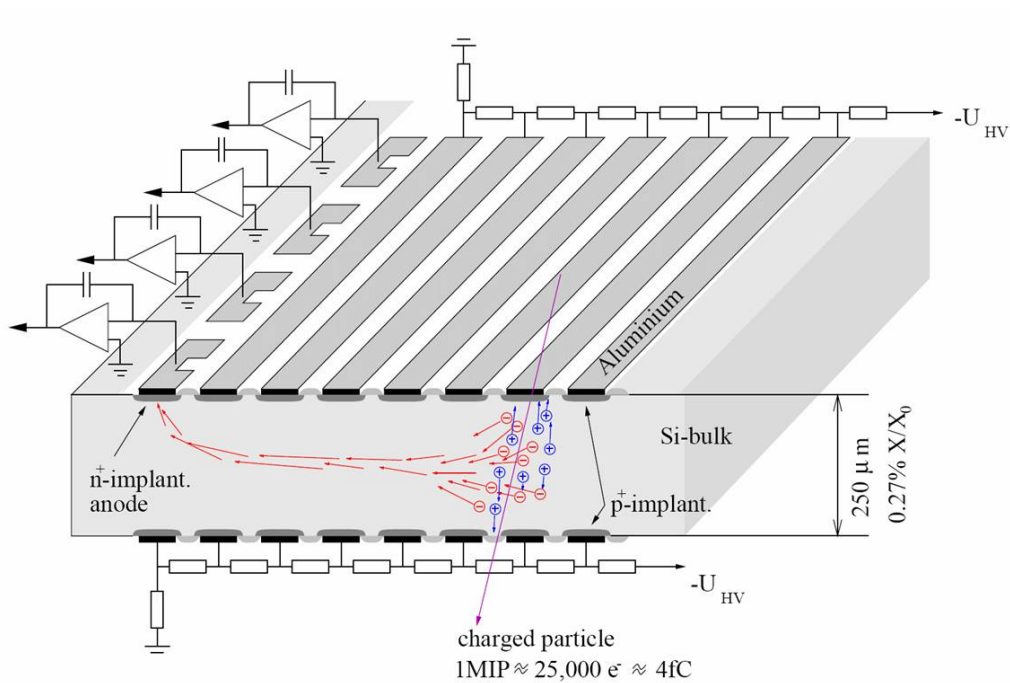
Figure 2.4: Operating mode of the silicon drift detectors.

$dN/d\eta$, and suppress conversion electrons. For more information see [H$^+$96, Slı03].
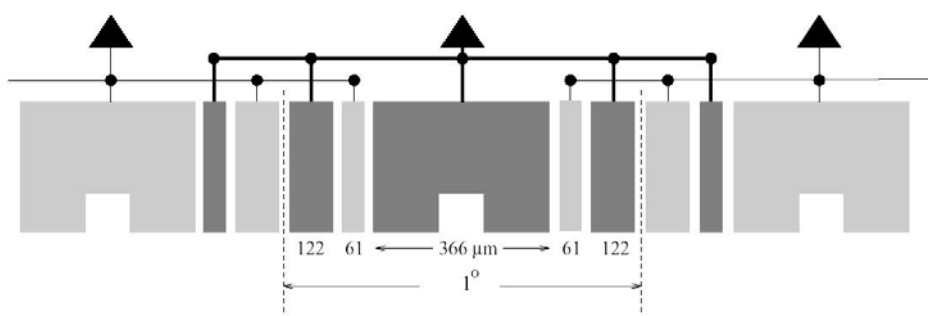
Figure 2.5: The layout of the interlaced structure of the readout pads used for drift silicon detectors. Each pad is divided into 5 pieces.

2.3   Ring Imaging Cherenkov Detectors

Two Ring Imaging Cherenkov detectors played an essential role in the CERES dilepton studies by providing electron identification. The Cherenkov radiation is emitted when a charged particle traverses a medium with refractive index n with a velocity v above the velocity of light c/n in that medium. The threshold condition is given by:

$$\beta_{th} = \frac{v_{th}}{c} \geq \frac{1}{n} \; . \tag{2.3}$$

The angle of emission increases with the velocity:

$$\theta_c = \arccos \frac{1}{n\beta} \; , \tag{2.4}$$

and reaches a maximum value for $\beta = 1$. The threshold velocity translates into a threshold energy $E_{th} = \gamma_{th}\, m_0\, c^2$ yielding:

$$\gamma_{th} = \frac{1}{\sqrt{1 - \beta_{th}^2}} = \frac{n}{\sqrt{n^2 - 1}} \; . \tag{2.5}$$

The number of Cherenkov photons emitted per unit path length dx is given by:

$$\frac{dN}{dx} = 2\pi\alpha z^2 \int \left(1 - \frac{1}{n^2\beta^2} \right) \frac{d\lambda}{\lambda^2} \tag{2.6}$$

for $n(\lambda) > 1$, where z is the electric charge of the passing particle, λ is the wavelength, and α the fine structure constant. The yield of Cherenkov radiation photons is proportional to $1/\lambda^2$, but only for those wavelengths where the refractive index is larger than $1/\beta$.

The CERES RICH detectors were filled with the gas mixture - 94% of Helium and 6% of Methane - at the atmospheric pressure. This choice of the gas mixture as a gas radiator assures that mainly electrons and positrons emit Cherenkov photons due to the high γ threshold ($\gamma_{th} \simeq 32$). This assumption should make RICH detectors almost hadron blind. However, the light hadrons has been recorded in the detectors above certain momentum. Both UV-detectors were filled with the TMAE (Tetrakis-di-Methyl-AminoEthylen) vapor in order to enhance the conversion of incoming photons to electrons via photo-ionization effect. In Fig. 2.6 the operating mode of the RICH1 detector is presented. A complete description of the RICH detectors one will find in [B$^+$94, B$^+$95]. The information from the RICH detectors were not used for this analysis.

2.4   Time Projection Chamber

The pad chamber was replaced by the Time Projection Chamber in 1998. This upgrade of the CERES experiment extended its detection capability from electrons to all charged particles.
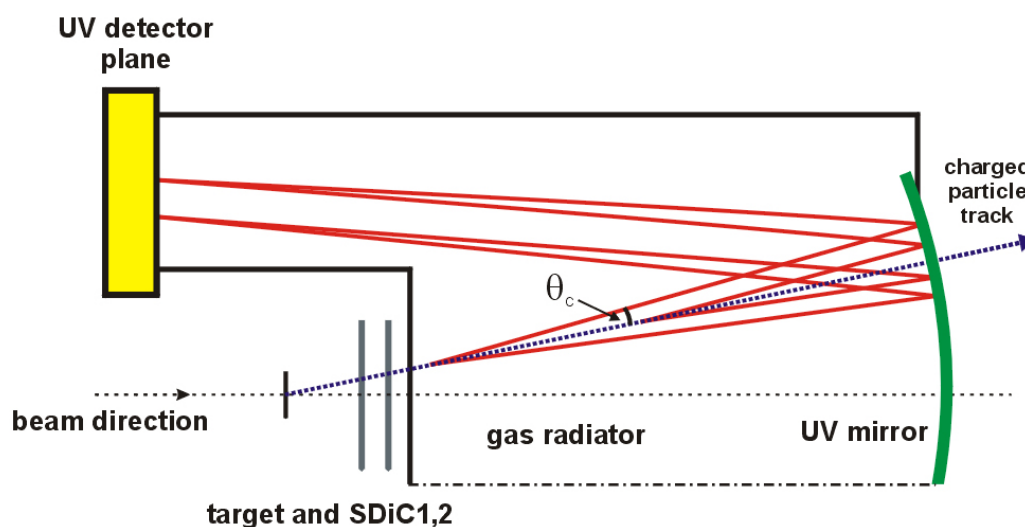
Figure 2.6: Schematic view of the CERES RICH1 detector with a spherical mirror. Produced Cherenkov photons are reflected by a spherical mirror and focused onto the photon detector placed at the focal point of the mirror.

The particle identification was accomplished in the TPC by the measurement of the particle charge, momentum, and energy loss dE/dx.

The Time Projection Chambers provide three-dimensional information about charged particles passing through the active volume of the detector. The capacity of the active volume is limited only by abilities to keep it at the uniform condition. The detector is essentially a large gas-filled cylinder with a high voltage electrode providing an electric drift field. Perpendicular to the drift field, arrays of multi-wire proportional chambers are arranged (read-out chambers). A charged particle passing through the medium produces electron-ion pairs along its path. In the presence of electric drift field liberated electrons drift toward the anode of the read-out chamber. Upon reaching the high field region, close to the anode wire, every electron is quickly accelerated and consequently produces an avalanche. The charge produced in the avalanche induces a signal on cathode pads which is recorded using charged sensitive amplifiers attached to the pad. Two coordinates of the liberated electrons are given by the position of the signal induced on the cathode pads. The third coordinate is given by the drift time of the ionization electrons. Since all ionization electrons created in the sensitive volume of the TPC will drift towards the MWPC, each anode wire over which the particle trajectory crosses will sample that portion of the track. This yields many space points for each track allowing the full reconstruction of the particle trajectory.

The CERES TPC is shown in Fig. 2.7. The azimuthal and polar coverage of the TPC matches the acceptance of the rest of the experimental setup. The drift field was radial and
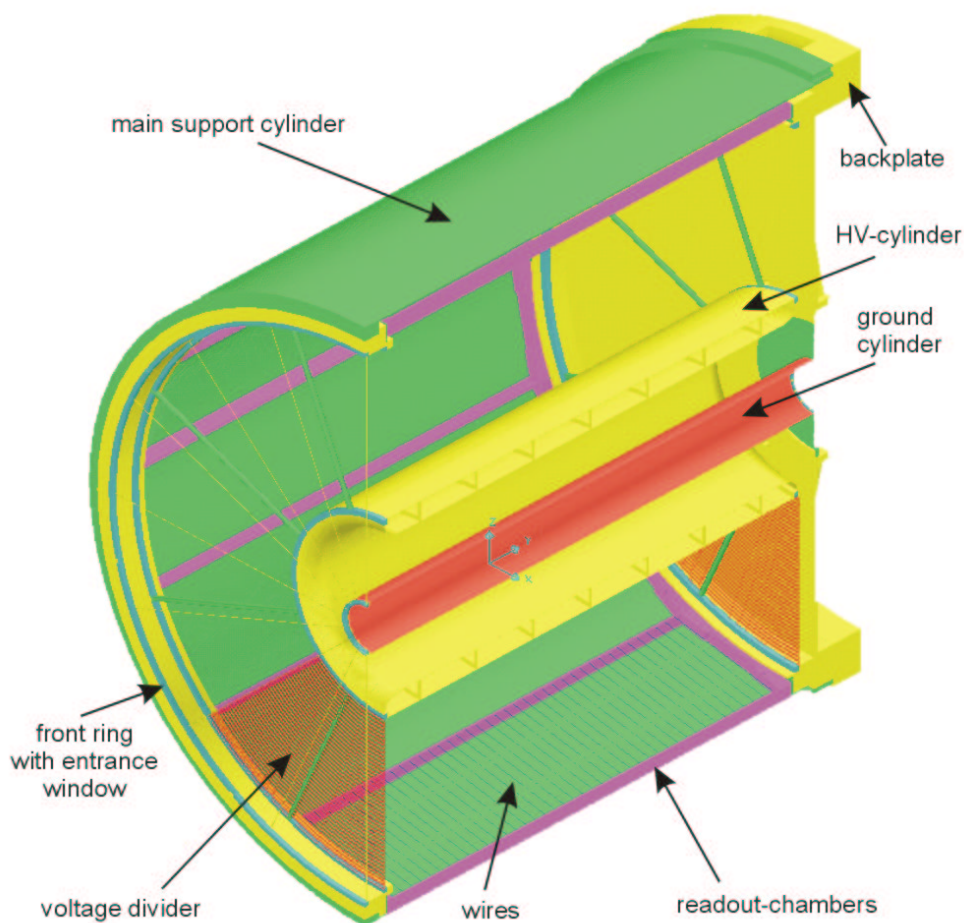
Figure 2.7: Schematic view of the CERES TPC.

the 16 readout chambers were arranged on the outer cylinder (R=130 cm), parallel to the beam direction in such a way that they formed a polygonal structure covering the full azimuthal acceptance. Additionally, the TPC was enclosed by the two opposite-polarity solenoidal coils resulting in an inhomogeneous magnetic field. This assured that a particle passing through an active volume of the detector will be deflected predominantly in the azimuthal direction. An active volume of 2 m length was divided into 20 planes providing up to 20 space points per measured track. The inner cylinder of radius of 48.6 cm was at a potential of -30 kV resulting in a $1/r$ dependence of electric field [GM02]. In order to make the electric field uniform in the beam direction both sides of the TPC were closed by 50 μm capton foils with 40 concentric copper rings. The rings were supplied with voltage by two voltage divider chains. The magnetic

field lines for the CERES TPC are indicated in Fig. 2.1 by red dotted lines. The TPC coordinate system is shown in Fig. 2.8. The origin of the coordinate system is in the centre of the SDD1. The z axis corresponds to the beam axis in the experiment. The $x - y$ plane is defined such that the x axis is at the boundary between chamber 15 and 0.

Figure 2.8: The coordinate system of the TPC.

2.4.1 Gas Properties

The choice of the gas mixture used in the proportional chambers is always individually optimized for the given experimental setup, and is governed by several factors: low working voltage, high gain, good proportionality, high rate capability, low diffusion, and low multiple scattering. Two main components of the gas mixture commonly used are a noble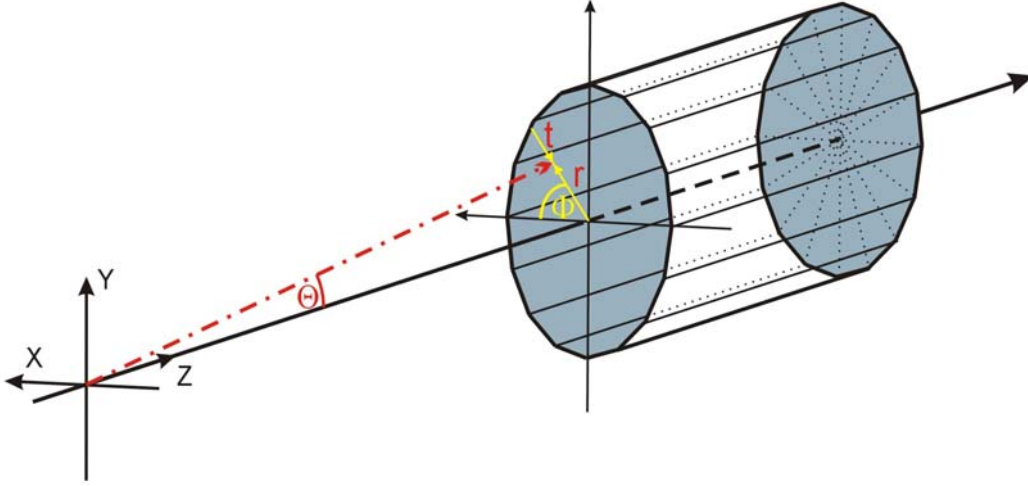 gas and so-called quencher. Noble gases are chosen due to the lowest electric field intensities required to form an avalanche. However, the proportional chamber only with the noble gas cannot be operated after the certain gain ($10^3 - 10^4$) due to continuous discharge caused by the high excitation energy of these elements. Exited noble gas atoms formed in the avalanche create high energy photons while they de-excite. Such photons are capable of ionizing the cathode and causing further avalanches. To stabilize the avalanches process some polyatomic gas (quencher) should be added (e.g. CO_2, CH_4, BF_3 ...). These molecules absorb the radiated photons and dissipate this energy through dissociation or elastic collisions.

The motion of charged particles under the influence of electric and magnetic field, $\overrightarrow{E}$ and $\overrightarrow{B}$, is described by the drift velocity vector $\overrightarrow{v_d}$, determined by the linear equation [BR94]

$$\frac{\overrightarrow{v_d}}{\tau} \frac{e}{m} - \left[\overrightarrow{v_d} \times \overrightarrow{B} \right] = \frac{e}{m} \overrightarrow{E} \ . \tag{2.7}$$

Here m and e are the mass and the electric charge of a particle, and $\tau = m/K$ characterizes the mean time between subsequent collisions of the particle moving through the medium. K describe the frictional force proportional to the drift velocity vector. Solution of this equation reads

$$\overrightarrow{v_d} = \frac{e}{m}\tau \left|\overrightarrow{E}\right| \frac{1}{1 + \omega^2\tau^2} \left(\hat{E} + \omega\tau[\hat{E} \times \hat{B}] + \omega^2\tau^2(\hat{E} \cdot \hat{B})\,\hat{B}\right) \tag{2.8}$$

where $\omega = (e/m)\,B$ is the cyclotron frequency of the electron. Here $\hat{E}$ and $\hat{B}$ denotes the unit vectors in the directions of the two fields. The drift direction is governed by the dimensionless parameter $\omega\tau$. The relation between the parameter $\omega\tau$ and the angle between $\overrightarrow{v_d}$ and $\overrightarrow{E}$ vector is given by

$$\omega\tau = \tan\alpha_L \tag{2.9}$$

where α_L is the Lorentz angle.

The CERES TPC filled with the gas mixture of 80% Ne and 20% of CO_2 [A$^+$96a, A$^+$96b] was operating at the atmospheric pressure. The gas gain was measured as $8\cdot10^3$, resulting in the electronic gain of 46 mV/fC. The drift velocity was varied between 0.7 and 2.4 cm/μs with the maximal drift time of about 71 μs. The relatively large radiation length of Neon gas minimized the effect of the multiple scattering and on the other hand provided enough electron-ion pairs as required by the CERES TPC. The choice of CO_2 as a quencher minimized the effect of the Lorentz angle which was caused by the characteristic arrangement of the magnetic field with respect to the radial electric field. Also, the diffusion of the electrons drifting towards the readout chambers was reduced resulting in an increase of the detector spatial resolution. Gas mixtures using CO_2 as a quencher are very sensitive to the changes of the ambient conditions. Therefore the monitoring of the gas properties has to be performed (see Section 2.4.2).

2.4.2   Readout and Control Systems

The CERES TPC readout system was based on the 16 MWPCs. Each chamber was divided into 20 planes in the beam direction with 48 cathode pads in the azimuthal direction. Three groups of the wires planes, the gating grid, the cathode and the anode, were mounted in the azimuthal direction above the readout pads. The gating grid wires plane, placed 12 mm above the chamber surface, was responsible for protecting the TPC from ions being produced during the avalanches as well as from free charges being induced apart from the triggered collision. The potential of the gating grid wires was $-70, -210, -70, -210, \ldots$V in the closed state and -140 V during a valid event. The grounded cathode wire plane was placed 6 mm above the readout pads and 3 mm above the anode wires. The anode wires of the diameter of 20 μm were on positive potential of about 1.3 kV resulting in a gas gain of about 10^4. The charge induced during the avalanche was collected by the Chevron–shaped pads cathode. The Chevron pad shape (see Fig. 2.9) was selected because of its efficient charge sharing in the azimuthal direction and was optimized to minimize the differential non-linearity [Sch98]. The measurement of the

charge sharing in the azimuthal direction showed that the charge was usually distributed over three pads, with size of 6×10.3 mm^2. The measured pad response function was approximated with a Gaussian function with a standard deviation of 0.5 pads. Each pad was connected to the
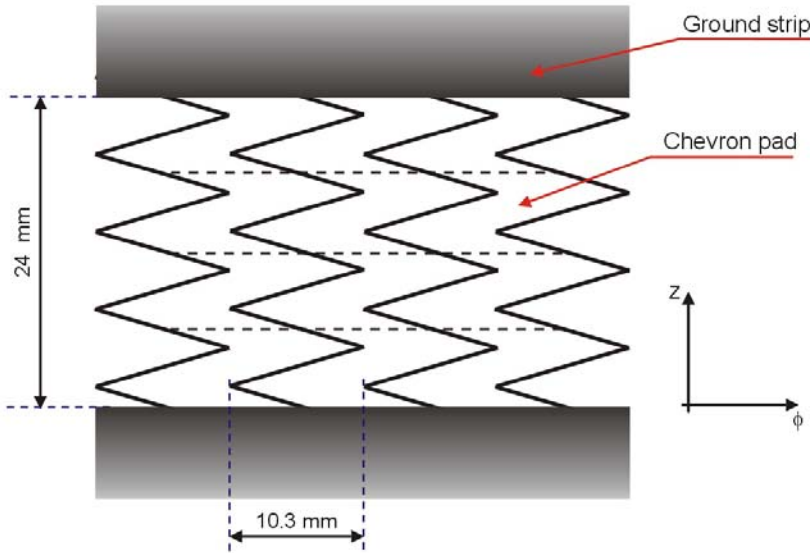

Figure 2.9: The layout of the CERES TPC pad plane. One readout channel was connected to four Chevron pads as indicated by the dashed lines. Chevron pads were separated by the ground plane strips in z direction.

charge amplifier and to an 8-bit ADC chip which sampled the analog signal in 256 times bins per channel, resulting in the total 4 million spatial points. For more detailed description of the readout electronic of the CERES TPC see [Til02].

The slow control of the TPC recorded periodically detector working conditions including the gas mixture, the pressure, the drift velocity, the temperature and the CO_2 contamination. Moreover, in order to keep the drift velocity variation below 0.1% the temperature of the TPC had to be stabilized as accurate as 0.2 K. To monitor the drift velocity in the CERES TPC, a gas monitor detector (**G**as pr**O**portional c**O**unter **F**or dr**I**fting **E**lectrons – GOOFIE) was used. In Chapter 3 the development of the new designed drift velocity monitor is presented. The latter will be implement into the gas system of the ALICE TPC.

In order to understand better the response of the CERES TPC, the laser track as a calibration system has been used. The laser system, based on a Nd:YAG laser, provided a low divergence laser beam with a wavelength of 1064 nm. To induce an ionization in the gas mixture used in the TPC, the wavelength of the laser was reduced to 266 nm. The position of the straight laser tracks was determined with spatial and time accuracy of 200 μm and 10 ns respectively. In Fig. 2.10 the perspective view of the TPC calibration system is show. Further information about the CERES TPC laser system can be found in [BMMZ98].
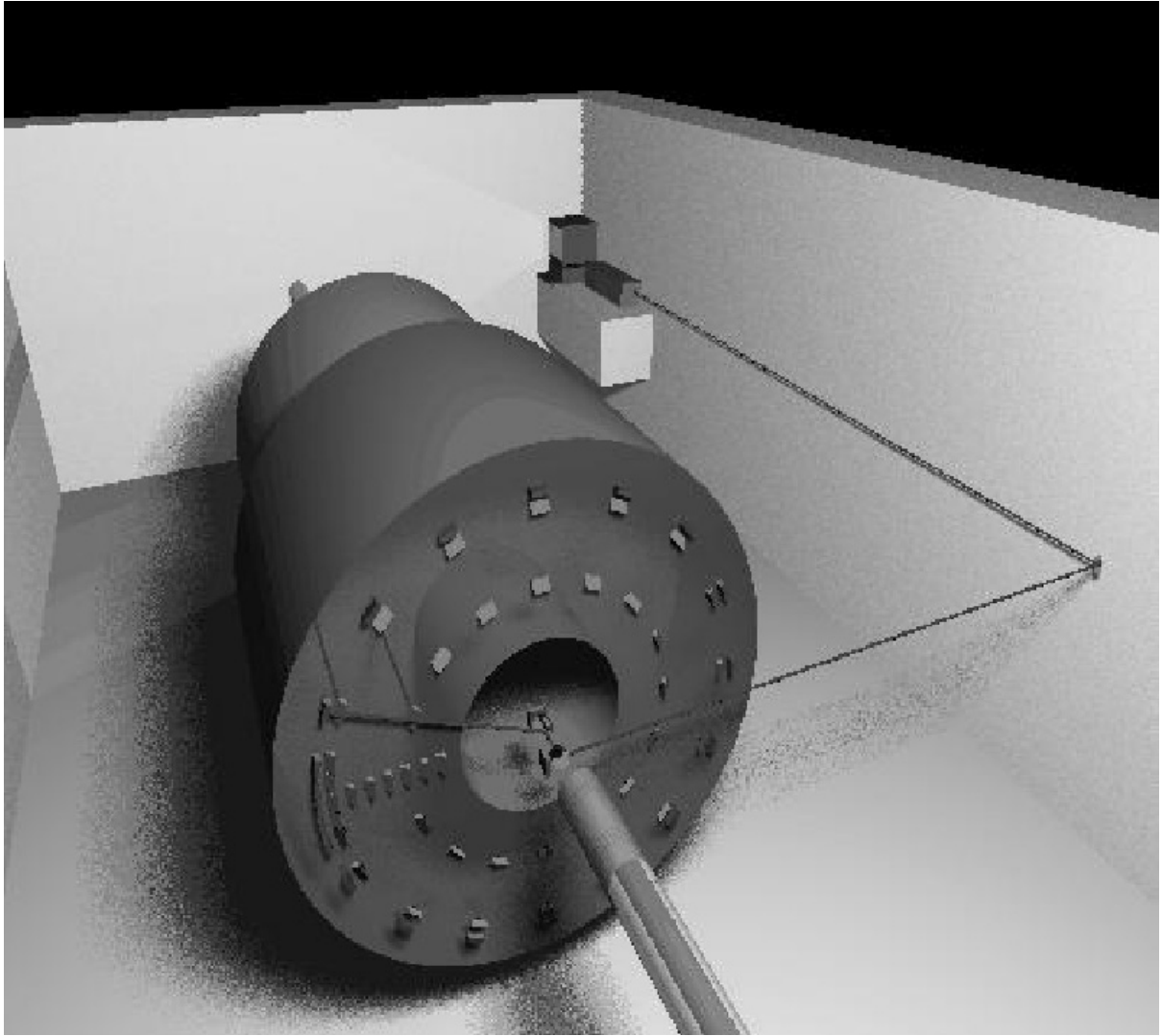
Figure 2.10: The perspective view of the CERES laser system.